ACS Catalysis

Research Article

pubs.acs.org/acscatalysis

Atomic Imaging of Carbon-Supported Pt, Pt/Co, and Ir@Pt Nanocatalysts by Atom-Probe Tomography

Tong Li,*[,†,‡] Paul A. J. Bagot,[†] Elvis Christian,[§] Brian R. C. Theobald,[§] Jonathan D. B. Sharman,[§] Dogan Ozkaya,[§] Michael P. Moody,[†] S. C. Edman Tsang,[⊥] and George D. W. Smith[†]

[†]Department of Materials, University of Oxford, Parks Road, Oxford OX1 3PH, United Kingdom

[‡]Australian Center for Microscopy and Microanalysis, and School of Aerospace, Mechanical & Mechatronic Engineering, The University of Sydney, Sydney, New South Wales 2006, Australia

[§]Johnson Matthey Technology Centre, Blount's Court, Sonning Common, Reading RG4 9NH, United Kingdom

[⊥]Wolfson Catalysis Centre, Department of Chemistry, University of Oxford, Oxford OX1 3QR, United Kingdom

Supporting Information

ABSTRACT: Atom probe tomography (APT) has been used to characterize commercially prepared Pt, Pt/Co alloy, and Ir@Pt core−shell nanoparticles supported on high-surface-area carbon black. Concentration profiles and 3D atom maps revealing the detailed internal structures and compositions of Pt, Pt/Co alloy, and Ir@Pt core−shell particles have been generated, and the distribution of trace impurity elements, including Na and Cl, has been examined. The observation of retained Na on the support, especially in the Pt nanoparticle system, indicates a more rigorous washing procedure is required. In the Pt/Co alloyed carbon-supported nanoparticle system, a marked variation in both compositions and particle sizes is observed. In the case of Ir@Pt, significant intermixing of the Ir core and Pt shell atoms takes place, which would be very difficult to measure by other techniques. All such observations will likely impact the catalytic performance of these materials. We envisage that the single nanoparticle analysis capability of APT, providing atomic-scale structures and chemical mapping, can also act as a means of quality control, identifying differences in the final product compared with the intended specification. Although the catalytic activity of these nanoparticles was not part of current study, the detailed information offered by such studies will permit knowledge-based improvements in nanoscale catalyst preparation methods and will also provide new ways of investigating structure and activity relationships at the nanometer scale.

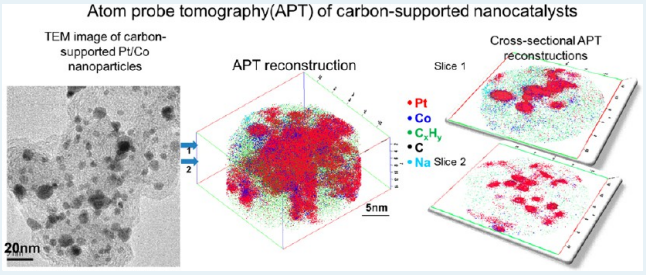

KEYWORDS: *atom probe tomography, platinum, platinum−cobalt alloyed particles, platinum−iridium core−shell nanoparticles, catalysts*

1. INTRODUCTION

Specific structures and morphologies of active phases can catalyze chemical reactions selectively, enabling the formation of desired products at high production rates.[1−3] The majority of commercial catalysts are solid state, taking the form of nanoparticles dispersed onto high-surface-area porous solids. In a large proportion of these catalysts, bimetallic systems containing two different metal species are particularly utilized. These demonstrate significantly improved activity, selectivity, and resistance to poisoning.[4−6] For example, in direct methanol fuel cells, the Pt catalyst component is highly effective in breaking C−O and C−H bonds, but Ru is also included, which greatly improves the resistance of the catalyst to carbon monoxide poisoning.[7,8]

Bimetallic nanoparticles can be roughly divided into two types of structures: alloyed structures, which incorporate a homogeneous chemical distribution of atoms within the nanoparticle, and core−shell structures, in which one metal forms the core of the nanoparticle and is surrounded by a shell of atoms of a different type. The final structures produced are dependent on synthesis methods and environment. This core−shell geometry shows particular tunable activity and selectivity. It is believed that electronic effects between the core and shell materials, which depend on core−shell dimensions, can markedly alter the electronic and adsorptive properties of the shell layer.[9] This suggests the possibility of nanoengineering of highly active morphologies if the core and shell structure and morphology can be controlled. Atomic-scale characterization of these core−shell interfaces will thus be critical to producing optimized nanoparticles for catalysis. In addition, catalyst nanoparticles are hosted on a support material, which not only maximizes the surface area of the particles but also actively contributes to the overall efficacy through metal−support interactions. The adsorptive properties of the support may also

Received: July 15, 2013
Revised: January 13, 2014
Published: January 14, 2014

influence the metallic active sites in close proximity. Being able to investigate the nature of these interactions is another important goal for the next generation of advanced catalysts.

Previous work has used an extensive range of characterization techniques, including transmission electron microscopy (TEM)[10−15] and associated high-angle annular dark field scanning TEM (HAADF-STEM);[16,17] X-ray diffraction (XRD);[12,14] and a number of spectroscopic methods, including X-ray photoelectron spectroscopy (XPS),[10,18,19] energy-dispersive X-ray spectroscopy (EDX),[10−14] and extended X-ray absorption fine structure spectroscopy (EXAFS).[14,20] Of particular interest to catalyst chemists is the simultaneous characterization of the chemical composition and structure of individual alloyed and core−shell nanoparticles at high resolution. This poses significant challenges for conventional characterization techniques. For example, XPS is a powerful technique for revealing the surface composition of nanoparticles, but it is hindered by the presence of polymers or surfactant stabilizers commonly used in the nanoparticle preparation, which present a thick organic layer coating obscuring useful signals. It is also known that the detectable depth of XPS is not entirely restricted to the top atomic surface, but may extend to a few nanometers below the surface, and thus, the depth resolution is somewhat limited.[21] Another quantitative technique, EDX, is also able to analyze the composition of the nanoparticles. Technically, the intensity of the X-rays is proportional to the concentration of each element in the particle. When the size of the bimetallic nanoparticles falls below 3 nm and their interatomic distances are similar, structural analysis is difficult to achieve in the normal mode of electron microscope operation. In addition, when the two elements of a core−shell nanoparticle have similar atomic weight, the contrast between them in HRTEM/HAADF is extremely difficult to differentiate.

Atom probe tomography (APT) is a microscopy technique that can provide 3D structure as well as chemical information at an atomic scale;[22,23] however, APT requires a very specific specimen geometry, needle-shaped with an end-tip radius of 30−100 nm. This requirement poses a significant obstacle for the analysis of supported or even unsupported nanoparticles to the extent that APT has until recently not been considered a viable option. Nevertheless, using an electrophoresis method to deposit nanoparticles from solution onto presharpened needle-shaped substrates, we recently demonstrated the potential of APT for the characterization of Ag(core)−Pd(shell) colloidal nanoparticle systems with a range of chemical compositions.[24] A clear and sharp interface between the core and shell was clearly indicated by the APT images, which also permitted quantitative measurements of the concentrations of each atomic species within the core and shell, respectively, as well as measurement of the thickness of the shell layers. In a further study, we have also characterized $CuZnGaO_x$ nanoparticles before and after reduction using APT, revealing very small but homogeneous Cu clusters in close proximity to larger Cu particles.[25] More recently Xiang et al.[26] attempted to produce a nanosize APT tip from catalyst powder by using a FIB (focused ion beam) to study CoCuMn core−shell particles, and Mountanabbir et al.[27] applied a site-specific lift-out technique by FIB to prepare APT samples from Al catalyzed Si nanowires. Note that the nanoparticles in the above studies were not dispersed onto any support materials, but were rather in the form of a colloidal dispersion or particle powders. In the present work, we have extended this electrophoresis technique to the study of supported catalyst materials. Pt, Pt/Co alloy, and Ir@Pt core−shell structured nanoparticles supported on carbon black have been characterized by APT and supporting TEM. These materials are important as low temperature fuel cell catalysts because of their favorable oxygen-reduction-reaction (ORR) activity and good corrosion stability.[13,28]

2. MATERIALS AND METHODS

Carbon-supported Pt, Pt/Co alloyed, and Pt(shell)−Ir(core) were supplied by Johnson Matthey PLC as prepared using an established wet chemical method.[28,29] Alloying of the Pt/Co catalysts was confirmed by the presence of a Pt_3Co phase using XRD analysis, and XPS analysis of Pt/Ir showed surface Pt enrichment compared with the bulk, indicating a successful coating of the Ir core with Pt. The nominal composition of Pt/Co alloyed and Pt−Ir core−shell particles is 74.7 atom % of Pt/25.3 atom % Co (37.9 wt % Pt and 3.88 wt % Co) and 29.3 atom % Pt/70.7 atom % Ir (14.0 wt % and 33.3 wt %), respectively. The metal loading of the three systems is 40%. The sizes of Pt, Pt/Co alloyed, and Pt−Ir core−shell particles measured by TEM are 7.0 ± 3.0, 5.6 ± 2.8, and 4.0 ± 1.8 nm, respectively, in Figure 1. TEM and HAADF-STEM examination was conducted using a JEOL 3000F operating at 300 kV.

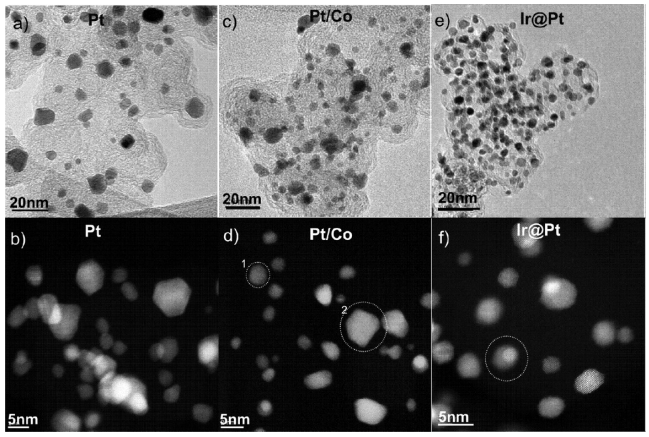

Figure 1. Low-resolution TEM images and HAADF-STEM images of (a, b) ∼7 nm diameter Pt nanoparticles on carbon support, (c, d) ∼6 nm diameter Pt/Co alloyed nanoparticles on carbon support, and (e, f) ∼4 nm diameter Ir@Pt core−shell nanoparticles on carbon support.

The sample preparation for the APT experiments is based on the principle of electrophoresis and has been applied to colloidal particle solutions, as detailed fully in our previous studies.[24,25] It was carried out on the second-stage sample polishing equipment (see the schematic presentation in Figure 2a). The carbon-supported nanoparticles powders were dissolved in a combination of water and methanol, and these nanoparticle solutions were then immersed in an ultrasonic bath for 15 minutes to obtain a good dispersion. Following this, a droplet of the solution was placed inside a gold wire loop and connected to a negative voltage bias. A relatively blunt (∼80−100 nm) presharpened APT tip was used as a substrate for deposition of the carbon-supported nanoparticles. A range of materials including W, Al, and Pt were explored as substrates, but only Pt and its alloys proved to retain the deposited nanoparticles with sufficient strength for APT analysis. This may be due to surface impurities, such as oxides, more readily forming on W and Al substrates compared with Pt.

dx.doi.org/10.1021/cs401117e | ACS Catal. 2014, 4, 695−702

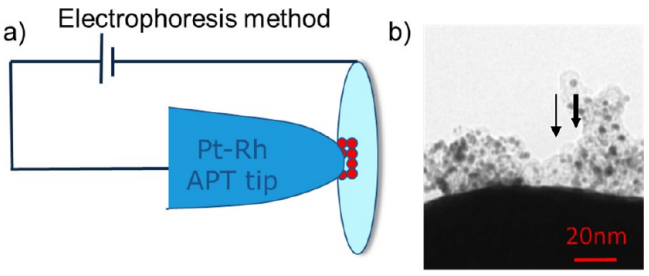

Figure 2. (a) Schematic representation of electrophoresis deposition method: positively charged nanoparticles deposited onto a Pt−Rh APT substrate, (b) Low resolution TEM image of ∼7 nm diameter Pt nanoparticles (indicated by larger arrow) on a carbon-supported surface, with ∼3−4 nm diameter nanoparticles (smaller arrow) on deeper internal porous carbon structure, both deposited on a blunt Pt−Rh APT substrate at 20 V for 20 s.

To aid distinction among the nanoparticles, all three of which contain Pt, and the substrate, a Pt−Rh alloy was chosen for this work. Hence, the detection of Rh during the APT analysis indicated the appearance of substrate. The Pt−Rh alloy was polished to form relatively blunt needle-shape specimens in a molten salt mixture ($4NaNO_3$/1NaCl volume) using Pt-22 atom % Rh wire (0.1 mm diameter, Alfa-Aesar), before being carefully cleaned with distilled water and then methanol. To deposit nanoparticles onto such samples by electrophoresis, each was in turn immersed in the polishing setup shown in Figure 2a), and when a positive voltage was applied, negatively charged nanoparticles were attracted to the Pt−Rh surface. Each sample was subsequently inspected in a TEM (Phillips CM20) to confirm deposition of a suitable layer of nanoparticles. A representative TEM image shown in Figure 2b demonstrates carbon-supported nanoparticles deposited using this electrophoresis method. For carbon-supported nanoparticles, close control of the number of deposited layers is less critical (but still important) than in previously used colloidal nanoparticle solutions because the former remain relatively well separated when deposited. Understanding this is central to enabling accurate atom probe analysis because multiple layers of spatially overlapping particles can be difficult to resolve in the APT data reconstruction. Nanoparticle concentration and size, along with pulsing voltage and pulsing duration, influence the deposition conditions. (As seen in SI1, the pulsing duration time was adjusted to avoid too few or too many nanoparticles deposited on the substrate.) In this study, typical conditions to deposit Pt, Pt/Co, and Ir@Pt were 15−20 V applied for around 15−20 s, using a Pt−Rh wire of approximately 80−100 nm end diameter.

The APT specimens were characterized using a Cameca LEAP 3000X-HR instrument. Several specimens were analyzed for each carbon supported nanoparticle system. The analyses were carried out in laser pulsing mode with a specimen temperature of 55 K, target evaporation rate of 2 ions per 1000 pulses, pulse rate of 160 kHz, and pulse energy of 0.45 nJ. The APT data was analyzed using the commercial IVAS 3.6.0 software. The reconstruction parameters (image compression factor and field factor[30]) are linked to the morphology and nature of the APT specimen. These parameters can be calibrated on the basis of crystallographic information in the data; however, no such information was available in this analysis. The difficulty in this study is that during the experiment, specimens do not maintain the model geometrical shape assumed by the reconstruction algorithm. Further, there was a nonuniform evaporation rate across the surface, which depends on the number and location of particles exposed at any instant. These issues made the standard procedures for the selection of reconstruction parameters unsuitable for these systems. The best way of optimizing reconstruction parameters was found to be based on correlating the sizes/shapes of nanoparticles in APT reconstructions with related TEM images. It was assumed that the image compression factor is 1, and the field factor was adjusted accordingly until a reasonable particle size/shape was achieved.

3. RESULTS AND DISCUSSION

3.1. Pt Nanoparticles. For comparison with the subsequent alloy particles studied and to verify the sizes of APT reconstructed nanoparticles, we first examine a simple arrangement of Pt nanoparticles on carbon black. This system is employed in polymer electrolyte fuel cells,[31] so it is also instructive from an application standpoint. To illustrate the starting morphology of the samples, Figure 2b shows a TEM image of the Pt nanoparticles, dispersed on the carbon support and attached to an APT Pt−Rh needle substrate. Interestingly, the average diameter of the Pt nanoparticles on top of the porous carbon is ∼7 nm. However, in deeper pores, there are considerably smaller Pt particles, around 3−4 nm in diameter, reflecting the differences in Pt deposition according to the pore location and dimensions. It can be seen that the nanoparticles are enveloped in a layer of adsorbed carbon- and hydrogen-containing compounds, which likely remain from the electrophoresis process used to deposit them onto this substrate. The same specimen was subsequently characterized using APT, and the reconstructed 3D images are presented in Figure 3. It should be noted that only a cylindrical subvolume of the tip in Figure 2b was analyzed by APT.

In the reconstructions, each dot represents the spatial coordinates of an individual ion (e.g., Pt^{2+}) or a complex ion species (e.g., CH_{1-3}^{+}, $C_2H_{1-7}^{1+}$, $C_3H_{1-11}^{1+}$, etc., which are fragments of the carbon support, surfactants from the synthesis, or the methanol solvent). The full 3D atom map in Figure 3a shows a complex overall morphology. The mass spectrum indicates the detection of Pt^{+}, Pt^{2+}, H_2O^{+}, groups of $C_xH_y^{+}$, C^{+}, and Na^{+} peaks (in Supporting Information Figure SI2). To clarify the atom map in Figure 3a, a better perspective can be achieved by examining thin (5 nm) slices through the data. Hence, Figure 3a was sectioned across the $X-Y$ plane at two distinct positions along the z axis, marked 1 and 2, and the results are presented in parts b−e, respectively, of Figure 3. In APT the z direction from top to bottom represents the sequential order of evaporation of the individual ions. Slice 1 (in the top part of Figure 3a) therefore represents the surface layer of the deposited carbon-supported Pt nanoparticles, and slice 2 shows the bottom layer. The APT reconstructions of Pt, C_xH_y, and Na ions in slices 1 and 2 are shown separately to clarify the positions of Pt and the carbon support. The positions of Pt ions alone shown in Figure 3b and d highlight the successful imaging of individual Pt nanoparticles. It is also apparent that there are substantial variations in nanoparticle size within this small volume, including relatively larger nanoparticles (7−8 nm diameter) in the top region and smaller nanoparticles (3−4 nm diameter) at deeper depths in the porous support. Thus, the size distribution corresponds well to the characterization by conventional TEM but gives a better-defined spatial view.

dx.doi.org/10.1021/cs401117e | ACS Catal. 2014, 4, 695−702

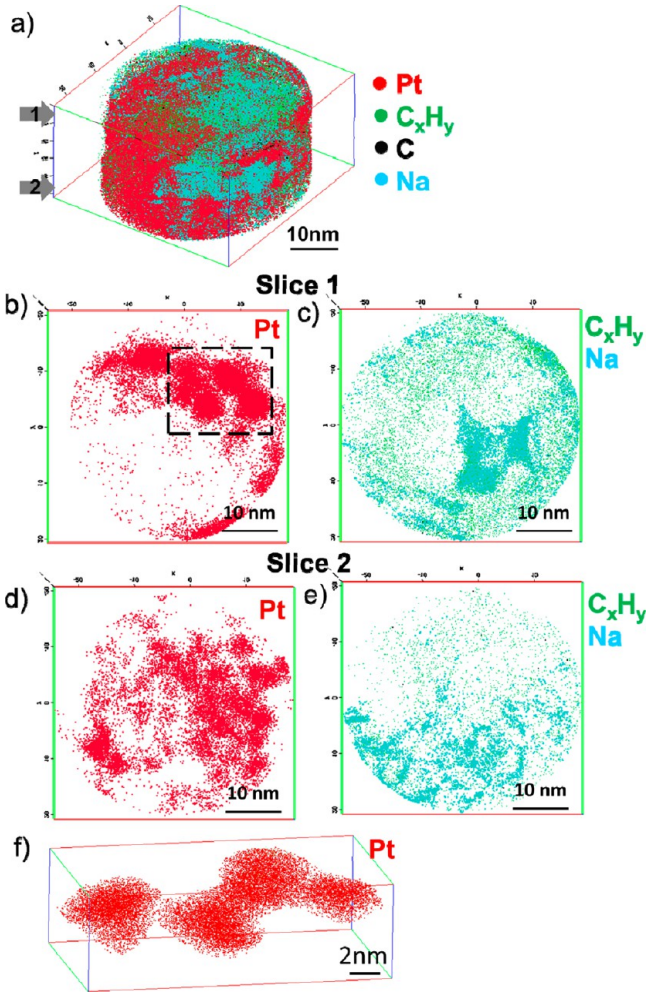

Figure 3. (a) APT reconstruction of Pt nanoparticles on carbon support showing all species, (b) APT reconstruction (X–Y view) of the top 5 nm cross-sectional region marked 1 in part a showing ~7 nm diameter Pt particles, (c) APT reconstruction (X–Y view) of slice 1 showing C_xH_y and Na, (d) APT reconstruction (X–Y view) of the bottom 5 nm cross-sectional region marked 2 in part a showing ~3–4 nm diameter Pt particles at deeper porous structure, (e) APT reconstruction (X–Y view) of slice 2 showing C_xH_y and Na, and (f) APT reconstruction of ~3–4 nm diameter Pt particles from the dashed rectangle box in part b. The Pt nanoparticles on carbon support were deposited onto the APT substrate at 20 V for 20 s.

Aside from the distribution of intended materials present in these supported catalysts, APT is highly sensitive to all elements in the local region analyzed and can therefore be used to look for trace impurities. The detection of Na (and trace Cl) ions is of significant importance. The original presharpened Pt–Rh APT samples without any nanoparticles deposited were separately analyzed. In this case, Na and Cl were not present on the surface. Furthermore, mass spectra from Pt–Rh samples following an unsuccessful deposition of carbon-supported Pt nanoparticles in water/methanol also reveal the lack of any Na and Cl (details in Supporting Information Figure SI2), and Na ions were detected only in association with C_xH_y complex species, not with Pt, as shown in Figure 3c and e. Therefore, it seems most probable that these impurities were introduced during the original synthesis, in which chloroplatinic acid (H_2PtCl_6) used as the Pt precursor is hydrolyzed by sodium bicarbonate during the wet impregnation process.[29] Their presence, even in trace quantities is well-known to cover active sites, which leads to attenuated activity as well as accelerating metal sintering. For example, there is evidence that Na can play a significant adverse role on catalyst performance for CO oxidation over Pt/Co.[32] Such species are intended to be removed by several cycles of washing. However, Figure 3c and d clearly indicates significant retention of Na^+ on the carbon support. Cl^- peaks, however, are only just detectable above the background noise level in the mass spectra, suggesting the washing stages have been more effective for its removal. Note that conventional chemical analysis, such as inductive coupling plasma (ICP) and EDX can also give trace elemental analysis, but to achieve such analysis at targeted atomic locations is extremely challenging. It is well-known that surface functional groups on activated carbon black carry negative charge as a result of the presence of phenolic or carboxylic groups (FTIR, not shown). Thus, the accumulation of Na^+ on the carbon support is attributed to the formation of electrostatic double layers on the carbon surface. Although these ions are shown to locate on the carbon surface, they can migrate to metal sites at elevated temperature. As a result, this analysis suggests a more drastic procedure to remove surface adsorbates such as sodium ions needs to be developed.

We also find that there are some low-density regions; for example, if the two APT reconstructions in Figure 3b and c or Figure 3d and e are superimposed. These are most likely due to the porous nature of the carbon support, which forms an incomplete coating onto the APT Pt–Rh substrate. For a closer look at some of the individual nanoparticles detected, the black rectangular region of interest highlighted in Figure 3b was isolated. The reconstruction of the four Pt nanoparticles present within this volume is shown in Figure 3f. These results confirm that high-resolution characterization of supported catalysts can be achieved using APT by combined elemental mapping and simultaneous morphological imaging.

3.2. Pt/Co Alloy Nanoparticles. Pt/Co alloyed nanoparticles on carbon supports were also examined by APT. This alloy system has been actively studied for use in proton-exchange membrane (PEM) fuel cells, in which the addition of Co improves durability.[32,33] Pt/Co is also employed as a selective catalyst in many industrial hydrogenation reactions.[34] As in the case of Pt on carbon, APT samples were prepared by electrophoretic deposition onto a Pt–Rh substrate. The average diameter of the alloyed particles measured by TEM was 5.6 ± 0.2 nm (see Figure 1c and d). A typical atom map revealing a cluster of these nanoparticles detected in APT is shown in Figure 4a. As in the previous section, to clarify the APT reconstructions, two thin cross sections marked "slice 1" and "slice 2" are generated across the X–Y plane. Slice 1 represents the upper surface layer nanoparticles deposited, and slice 2 represents a deeper layer. Figures 4b and 3d show x–y views of all species in the cross sections together with Pt isodensity surfaces (22.0 atoms/nm^3). The Pt and Co ions contained within Pt isodensity surfaces are shown in Figure 4c and e. These figures demonstrate the particle diameters to be in the range 2–4 nm, matching the information from Figure 1c and d. The particle labeled "1" in Figure 4b was itself isolated, and the reconstruction of this alone is shown in Figure 4f. From this individual particle, a 1D concentration profile was generated, Figure 4g. This yields an average particle composition of 93.1 ± 1.7 atom % Pt and 6.9 ± 0.5 atom % Co and also indicates that the particle has a homogeneous alloyed internal structure throughout. A STEM/EDX line analysis of a different particle

dx.doi.org/10.1021/cs401117e | ACS Catal. 2014, 4, 695–702

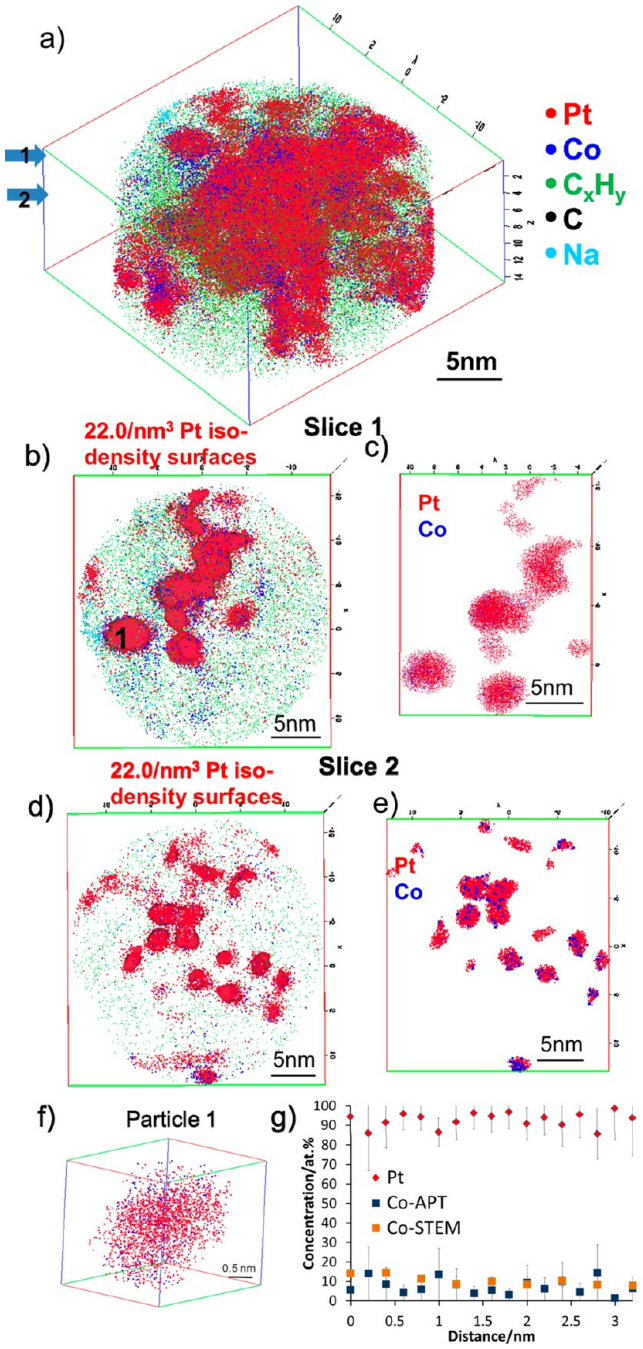

Figure 4. (a) APT reconstruction of Pt/Co nanoparticles on carbon support with all species, (b) APT reconstruction of the top 3 nm cross-sectional region marked 1 in part a showing all speices and Pt isodensity surfaces (53.0/nm^3), (c) APT reconstruction of Pt/Co nanoparticles inside Pt isodensity surfaces in part b, (d) APT reconstruction of region 2 (z = 7.8−8.6 nm) marked in part a showing all species Pt isodensity surfaces (53.0/nm^3), (e) APT reconstruction of Pt/Co nanoparticles inside Pt isodensity surfaces in part d, (f) particle 1 marked 1 in part b, and (g) 1D concentration profile of particle 1 in part f and separate STEM/EDX line analysis of particle 1 in Figure 1d for comparison. The Pt/Co nanoparticles on carbon support were deposited onto the APT substrate at 20 V for 15 s.

(∼4−5 nm) labeled "1" in Figure 1d is also plotted in Figure 4g, revealing an alloyed structure of Pt and Co with an average Co concentration of 9.4 ± 2.3 atom %.

Because of the high weight loading of Pt/Co nanoparticles (40%), they are relatively closely spaced in the atom maps. It is therefore challenging to precisely define the physical boundary for all nanoparticles, which may also be attributed to possible agglomeration. Hence, in this study, detailed composition measurements are restricted to those nanoparticles that are well-defined and separated from their surroundings, a procedure demonstrated in Figure 5a. The separated Pt/Co

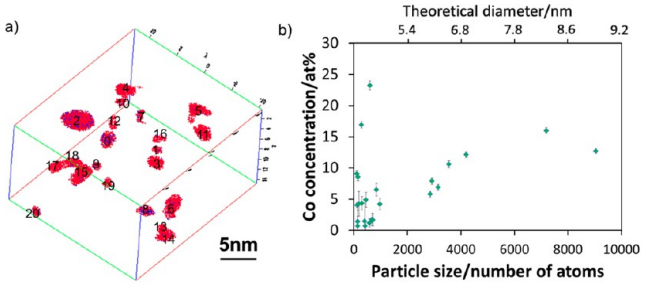

Figure 5. (a) Isolated Pt/Co nanoparticles from Figure 4a and the concentration of the numbered Pt/Co particles summarized in Supporting Information Figure SI3 and (b) Co concentration versus particle size (number of atoms) and theoretical particle diameter size (nm) of all separated Pt/Co nanoparticles in three data sets.

nanoparticles are numbered for identification, and a table of the concentration of individual nanoparticles is summarized in Supporting Information Figure SI3. Over three different APT data sets, the Co contents of a number of isolated nanoparticles are plotted versus their size in Figure 5b. The upper x axis in Figure 5b is theoretical particle diameter size in nanometers calculated from the number of counts and the theoretical density detected by atom probe (24 atoms/nm^3) on the basis of the assumption that all the particles are spherical and evaporated with the same detection efficiency (∼0.37). The results reveal marked variations in Co content and also show a size-dependence on composition. The average Pt and Co concentrations measured over all isolated particles are 93.7 ± 5.8 atom % and 6.3 ± 5.8 atom %, respectively across the three data sets.

The nominal composition of this industrially prepared Pt/Co alloy sample was 74.7 atom % Pt/25.3 atom % Co from ICP analysis. Individual particles have compositions ranging from almost pure Pt to those with Co contents of ∼25 atom %, comparable to the average value obtained from ICP analysis. However, STEM/EDX line analysis in Figure 4g demonstrated that a particle with a size of 4−5 nm had a lower Co concentration, consistent with APT results. Furthermore STEM/EDX line analysis of the particle labeled "2" in Figure 1d (∼10−12 nm) shows an average Co concentration of 30.1 ± 7.1 atom %. From looking at a range of particles in a size range of either 6−9 nm or 10−12 nm, STEM/EDX analysis revealed an average Co concentration of 24.6 ± 3.5 atom % in the smaller ones, and 31.5 ± 1.23 atom % in the larger. Therefore STEM/EDX confirms that there is a variation in Co concentrations across the nanoparticles that is linked to their sizes. Although the EDX method has limitations in terms of its accuracy, the variation of Co concentration with particle size is clear. The discrepancy between the average Co concentrations from APT/EDX data and that from the ICP analysis could be attributed to a number of possible reasons, each of which needs to be explored independently to determine the extent of its role. It does, however, suggest that there may be scope for

dx.doi.org/10.1021/cs401117e | ACS Catal. 2014, 4, 695−702

improving the wet impregnation method used to better mix the metals. For example, it is known that Co atoms tend to adhere more strongly to the phenolic and carboxylic surface functionalities, thus leading to variations in the alloy composition and phase segregation on the support.

A factor that may influence the APT result is associated with the electrophoresis sample preparation method. In this, we make the assumption that the particles attracted to the sample apex are a representative subset of the full range synthesized. However, the rate of migration of charged colloidal particles in an electric field depends (inversely) upon their size (and also upon their charge). For Pt−Co particles, a further consideration is that this material can be magnetic, and this property makes Pt−Co actively researched for magnetic information storage. The magnetic nature of Pt−Co is importantly dependent on the composition. Using the phase diagram obtained in a recent neutron scattering study,[35] we see that the transition point at 300 K from ferromagnetic to paramagnetic for a disordered alloy lies around 12 atom % Co. Particles with Co contents greater than this will be ferromagnetic and will consequently tend to agglomerate in solution under the influence of the electromagnetic fields present in the sample preparation. This is also a size-dependent phenomenon, with the largest magnetic forces generated in the bigger particles. Inspection of the data in Figure 4b reveals that for the largest particles analyzed, the determined Co content never exceeds around 16 atom %, which is entirely consistent with the argument that large, high-Co-content particles do not attach to the APT needle substrates. This does not in any way affect the significance of APT analysis of the detected particles because the catalytic activity of differently sized particles with substantial disparities in composition is likely to vary considerably. However, it clearly suggests that for future experiments (and, indeed, any possible catalyst preparation methods), such behavior needs to be taken into account for this particular system.

3.3. Ir@Pt Core−Shell Nanoparticles. Finally, we consider carbon-supported Ir@Pt core−shell particles. These elements combined in a core−shell morphology show considerable promise for PEM fuel cells.[36,37] For high-resolution characterization of this system, a significant problem exists for TEM in terms of resolving the two different metals because Pt and Ir have similar atomic weights. This makes the desired characterization of composition and thickness of the core and shell in Ir@Pt systems challenging. Previous work using XPS has indicated a clear enrichment in Pt compared with the bulk,[28] whereas recent APT investigations have demonstrated its suitability for colloidal Ag@Pd nanoparticles,[24] which have similar mass discrimination problems for TEM.

Unlike Pt and Pt/Co, in which electrophoresis of the dispersed catalyst materials produced deposits on the APT sample containing carbon-supported metallic nanoparticles, only isolated Pt(shell)−Ir(core) nanoparticles were deposited for this material. Three examples from three data sets are illustrated in Figure 6. The diameter of the Ir@Pt nanoparticles measured in TEM was 4.0 ± 0.2 nm, as shown in Figure 1e and f. In the APT reconstructions of Figure 6, particles of comparable sizes are evident. Some clearly show signs of a core−shell structure, but others appear to consist mainly of Pt. The mass spectrum in Figure 6b obtained from particle 1 in Figure 6a demonstrates that Pt^{2+} and Ir^{2+} peaks are well discriminated in the APT data. The reconstruction of this

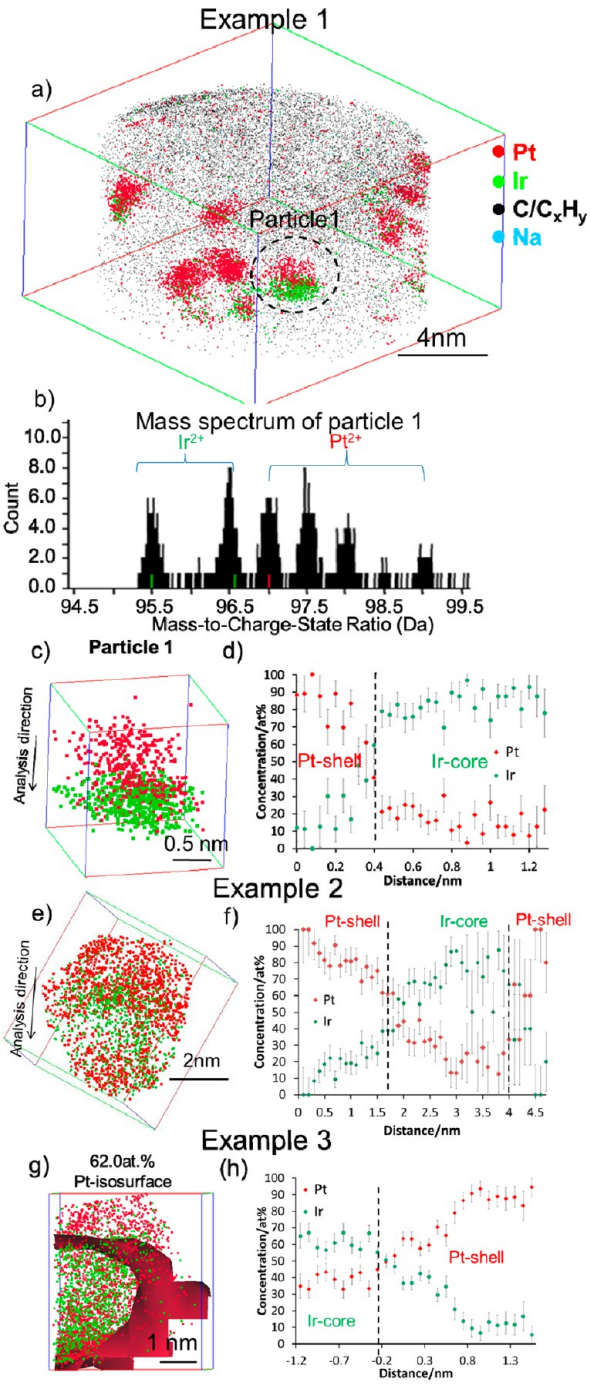

Figure 6. (a) Example 1: APT reconstruction of Ir@Pt nanoparticles with all species, (b) mass spectrum of particle 1 marked in part a, (c) APT reconstruction of particle 1, and (d) 1D concentration profile along the analysis direction marked as a black arrow in part c. (e) Example 2: APT recontrcution of Ir@Pt nanoparticle in other data set and (f) 1D concentration profile along the analysis direction marked in part e. (g) Example 3: APT reconstruction of Ir@Pt nanoparticle from separate data set with 62.0 atom % Pt isoconcentration surface and (h) concentration profile from Ir-core to Pt-shell (from proximity histograms obtained from the particle in part g). The Ir@Pt nanoparticles on carbon support were deposited onto the APT substrate at 15 V for 15 s.

particle is presented in Figure 6c. It shows a duplex structure rather than a complete core−shell morphology, with an ∼0.4 nm thick Pt-rich layer in direct contact with a thicker Ir-rich

dx.doi.org/10.1021/cs401117e | ACS Catal. 2014, 4, 695−702

Table 1. Concentrations of Shell and Core of Pt(shell)-Ir(core) Carbon-Supported Nanoparticles

	shell compositions (Pt−Ir)/at. %	core compositions (Pt−Ir)/at. %
particle 1	81 ± 5 to 19 ± 2	22 ± 5 to 78 ± 9
particle 2	75 ± 11 to 25 ± 5	30 ± 3 to 70 ± 5
particle 3	87 ± 8 to 13 ± 3	38 ± 3 to 62 ± 3
particle 4	69 ± 9 to 31 ± 6	13 ± 6 to 87 ± 17

region. The associated 1D concentration profile in Figure 6d (measured along the direction of black arrow in Figure 6c) reveals the composition of the Pt-rich and Ir-rich layers to be 81 ± 5 atom% Pt-19 ± 2 atom% Ir and 22 ± 5 atom% Pt- 78 ± 9 atom% Ir, respectively. Examples 2 and 3 in Figure 6e and g indicate more complete Pt(shell)−Ir(core) structures from two separate data sets. The concentrations measured from the profiles in Figures 6f and h along with a further example (not shown) were summarized in Table 1.

These observations clearly indicate variations in both core and shell contents between different particles of comparable sizes and, furthermore, demonstrate an apparent mixing of the elements in both layers. On average, the shell has a Pt content of 80 ± 8 atom %, with the core containing 77 ± 11 atom % Ir. This level of chemical information is not possible to extract from the typical HAADF-STEM and bright field STEM images in Figure 1f because of poor contrast between metal species with similar electron densities and the same fcc crystal structure.

The preparation of these Ir@Pt core−shell particles is based on a proprietary industrial method in which the Pt is deposited selectively on 4 nm Ir nanoparticles supported on carbon in a hydrogen environment. The in-house electrochemical testing and characterization (cyclic-voltammetry and IR) indicated a Pt-rich surface instead of a typical Pt−Ir mixed alloy.[28] Here, it is demonstrated that significant intermixing of the Ir core and Pt shell atoms has taken place. Thus, the APT data can be used as a means of quality control, identifying differences in the final product compared with the intended core−shell structure. Such discrepancies will certainly influence the catalytic activity of the Ir@Pt nanoparticles.

In interpreting the data, we are cautious that possibly, there may be trajectory aberrations and artifacts induced by uneven evaporation among the nanoparticles, the carbon support, hydrocarbons, and water because this sample geometry/structure is particularly challenging to study by APT. These features may lead to shape distortion of the nanoparticles along the z direction, although their general morphology matches well with the TEM images that play a valuable role in verifying particle shape/size. In the future, a thin layer of metal could be coated on top of the whole APT specimen, with the intention of encapsulating the full sample volume to reduce the potential of any reconstruction artifacts. TEM tomography correlated with APT data will also help to improve the data reconstruction.

4. CONCLUSIONS

In this study, we have demonstrated that APT can be successfully applied to the characterization of carbon-supported metal nanoparticles, importantly in the same form as those used for actual catalytic processes. Using this technique, we have shown a wealth of new information that is inaccessible by current alternative methods. The structures, compositions, and 3D spatial distributions of three types of nanoparticles on carbon supports were analyzed by APT. A significant amount of Na was found to remain on the carbon support surface (along with trace amounts of Cl) in the Pt nanoparticle system. Information of this kind is directly relevant to the understanding and improvement of commercial catalyst preparation procedures; in this case, a more thorough approach to remove these surface adsorbates is required. The analysis of the Pt/Co alloy particle system demonstrates a marked variation of compositions and sizes, which is consistent with results obtained by STEM. This information strongly suggests that the intended homogeneous distribution in both was not achieved and that an average concentration value by ICP is insufficient to properly correlate concentration with activity. Finally, the APT analysis of Ir@Pt core−shell nanoparticles reveals significant intermixing of the Ir core and Pt shell atoms, a key detail that would not be possible to obtain from other techniques, such as HAADF-STEM. The conspicuous discrepancies between our observations and the intended structures in all three systems confirm detailed atomic-scale chemical information is vital to understanding the relationship between structure and catalytic efficiency. In future work, improved APT sample preparation and data reconstruction methods are required to image "aggregated" nanoparticles to carry out a more rigorous assessment of composition versus particle size. In addition, linking this type of high-end characterization with activity tests will allow more rapid evaluation of nano-engineered catalytic nanoparticles for a wide variety of applications.

■ ASSOCIATED CONTENT

Supporting Information

Supporting data as noted in the text, SI1 and SI2 for TEM image and STEM/EDX analysis of carbon-supported Pt/Co nanoparticles respectively. This material is available free of charge via Internet at http://pubs.acs.org.

■ AUTHOR INFORMATION

Corresponding Author

*E-mail: tong.li@sydney.edu.au.

Notes

The authors declare no competing financial interest.

■ ACKNOWLEDGMENTS

We thank Johnson Matthey for providing the carbon-supported metal, alloy, and core−shell samples for APT characterization. The access of TEM microscopy facilities at both Johnson Matthey Technology Centre and Birmingham University is also kindly acknowledged. Prof. Chris Grovenor at Oxford Materials is also thanked for his support. This work was supported by the UK Engineering and Physical Sciences Research Council (EPSRC) under Grant No. EP/077664/1.

■ REFERENCES

(1) Bowker, M. *The Basis and Applications of Heterogeneous Catalysis*; Oxford University Press: Oxford, 1998.
(2) Bell, A. T. *Science* **2003**, *299*, 1688−1691.

(3) Kolasinski, K. K. *Surface Science: Foundations of Catalysis and Nanoscience*; John Wiley&Sons: Chichester, 2012.
(4) Sinfelt, J. H. *Sci. Am.* **1985**, *253*, 90−95.
(5) Rodriguez, J. A.; Goodman, D. W. *Science* **1992**, *257*, 897−903.
(6) Chen, J. G.; Menning, C. A.; Zellner, M. B. *Surf. Sci. Rep.* **2008**, *63*, 201−254.
(7) Watanabe, M.; Motoo, S. *J. Electroanal. Chem.* **1975**, *60*, 267−273.
(8) Watanabe, M.; Motoo, S. *J. Electroanal. Chem.* **1975**, *60*, 275−283.
(9) Kitchin, J. R.; Nørskov, J. K.; Barteau, M. A.; Chen, J. G. *Phys. Rev. Lett.* **2004**, *93*, 156801−1−15608−4.
(10) Jayasayee, K.; Dam, V. A. T.; Verhoeven, T.; Celebi, S.; de Bruijn, F. A. *J. Phys. Chem. C* **2009**, *113*, 20371−20380.
(11) Sobal, N. S.; Ebels, U.; Möhwald, H.; Giersig, M. *J. Phys. Chem. B* **2003**, *107*, 7351−7354.
(12) Qian, Y.; Wen, W.; Adcock, P. A.; Jiang, Z.; Hakim, N.; Saha, M. S.; Mukerjee, S. *J. Phys. Chem. C* **2008**, *112*, 1146−1157.
(13) Paulus, U. A.; Wokaun, A.; Scherer, G. G.; Schmidt, T. J.; Stamenkovic, V.; Radmilovic, V.; Markovic, N. M.; Ross, P. N. *J. Phys. Chem. B* **2002**, *106*, 4181−4191.
(14) Lai, F.-J.; Sarma, L. S.; Chou, H.-L.; Liu, D.-G.; Hsieh, C.-A.; Lee, J.-F.; Hwang, B.-J. *J. Phys. Chem. C* **2009**, *113*, 12674−12681.
(15) Gontard, L. C.; Dunin-Borkowski, R. E.; Ozkaya, D. *J. Microsc.* **2008**, *232*, 248−259.
(16) Chen, S.; Ferreira, P. J.; Sheng, W.; Yabuuchi, N.; Allard, L. F.; Shao-Horn, Y. *J. Am. Chem. Soc.* **2008**, *130*, 13818−13819.
(17) Heggen, M.; Oezaslan, M.; Houben, L.; Strasser, P. *J. Phys. Chem. C* **2012**, *116*, 19073−19083.
(18) Salvatore Aricò, A.; Stassi, A.; Gatto, I.; Monforte, G.; Passalacqua, E.; Antonucci, V. *J. Phys. Chem. C* **2010**, *114*, 15823−15836.
(19) Tao, F.; Grass, M. E.; Zhang, Y.; Butcher, D. R.; Renzas, J. R.; Liu, Z.; Chung, J. Y.; Mun, B. S.; Salmeron, M.; Somorjai, G. A. *Science* **2008**, *322*, 932−934.
(20) Sinfelt, J.; Via, G.; Lytle, F. *J. Chem. Phys.* **1982**, *76*, 2779−2789.
(21) Briggs, D.; Seah, M. P. *Practical Surface Analysis by Auger and X-ray Photoelectron Spectroscopy*; Briggs, D., Seah, M. P., Eds.; John Wiley & Sons: Chichester, 1983.
(22) Miller, M. K.; Smith, G. D. W. *Atom Probe Microanalysis: Principles and Applications to Materials Problems*; Materials Research Society: Pittsburgh, PA, 1989.
(23) Miller, M. K. L.; Forbes, R. G. *Mater. Charact.* **2009**, *60*, 461−469.
(24) Tedsree, K.; Li, T.; Jones, S.; Chan, C. W. A.; Yu, K. M. K.; Bagot, P. A. J.; Marquis, E. A.; Smith, G. D. W.; Tsang, S. C. E. *Nat. Nanotechnol.* **2011**, *6*, 302−307.
(25) Yu, K. M. K.; Tong, W.; West, A.; Cheung, K.; Li, T.; Smith, G.; Guo, Y.; Tsang, S. C. E. *Nat. Commun.* **2012**, *3*, 1230−1236.
(26) Xiang, Y.; Chitry, V.; Liddicoat, P. V.; Felfer, P.; Cairney, J.; Ringer, S. P.; Kruse, N. H. *J. Am. Chem. Soc.* **2013**, *135*, 7114−7117.
(27) Moutanabbir, O.; Isheim, D.; Blumtritt, H.; Senz, S.; Pippel, E.; Seidman, D. N. *Nature* **2013**, *496*, 78−82.
(28) Gyenge, E.; Atwan, M.; Northwood, D. *J. Electrochem. Soc.* **2006**, *153*, A150−A158.
(29) Keck, L.; Buchanan, J. S.; Hards, G. A. U.S. Patent 5068161, 1991.
(30) Gault, B.; De Geuser, F.; Stephenson, L. T.; Moody, M. P.; Muddle, B. C.; Ringer, S. P. *Microsc. Microanal.* **2008**, *14*, 296−305.
(31) Zhang, J. *PEM Fuel Cell Electrocatalysts and Catalyst Layers: Fundamentals and Applications*; Springer: London, 2008.
(32) Kwak, C.; Park, T.-J.; Suh, D. J. *Appl. Catal., A* **2005**, *278*, 181−186.
(33) Yu, P.; Pemberton, M.; Plasse, P. *J. Power Sources* **2005**, *144*, 11−20.
(34) Bertero, N. M.; Trasarti, A. F.; Moraweck, B.; Borgna, A.; Marchi, A. J. *Appl. Catal., A* **2009**, *358*, 32−41.
(35) Mehaddene, T.; Kentzinger, E.; Hennion, B.; Tanaka, K.; Numakura, H.; Marty, A.; Parasote, V.; Cadeville, M. C.; Zemirli, M.; Pierron-Bohnes, V. *Phys. Rev. B.* **2004**, *69*, 024304-1−024304-13.
(36) Ramirez-Caballero, G. E.; Balbuena, P. B. *Chem. Phys. Lett.* **2008**, *456*, 64−67.
(37) Karan, H. I.; Sasaki, K.; Kuttiyiel, K.; Farberow, C. A.; Mavrikakis, M.; Adzic, R. R. *ACS Catal.* **2012**, *2*, 817−824.